Role of microscopic coherent force and hot-carrier cooling in photoinduced phase transition for chalcogenide phase-change materials

Li Chen (陈立),[1] Liyuan Chen (陈丽媛),[1] Hongli Chen (陈红丽) ●,[1] Yawei Li (李亚巍),[1] Liyan Shang (商丽燕) ●,[1]
Liangqing Zhu (朱亮清),[1] Jinzhong Zhang (张金中),[1] Shijing Gong (龚士静),[1] and Zhigao Hu (胡志高) ●[1,2,*]

[1]*Technical Center for Multifunctional Magneto-Optical Spectroscopy (Shanghai),*
Engineering Research Center of Nanophotonics and Advanced Instruments (Ministry of Education),
Department of Physics, School of Physics and Electronic Science, East China Normal University, Shanghai 200241, China
[2]*Collaborative Innovation Center of Extreme Optics, Shanxi University, Taiyuan, Shanxi 030006, China*

The nonequilibrium ultrafast carrier dynamics of the photoinduced phase transition in chalcogenide phase-change material (rocksalt Ge-Sb-Te) has been investigated via real-time time-dependent density-functional theory, reproducing experimental observations of subpicosecond timescales and electronic diffraction. We develop a picture of the photocarrier distribution in momentum and real space dependent on the laser external field, revealing that thermal and coherent phonons contend to modulate the crystalline order. Localized coherent Peierls suppression intensifies with electronic excitation, and ultrafast dissipation of antibonding electrons near the Fermi surface incubates Lindemann particles. Full-domain hot-carrier excitation upon intense photon scattering cools and participates in the self-amplified growth of molten particles, followed by a sustained nonradiative recombination of photoelectron and photogenerated hole pairs. These findings present a comprehensive and definitive energy landscape for the nonequilibrium phase engineering in chalcogenide phase-change materials.

I. INTRODUCTION

The decoupling of lasers from multiple degrees of freedom (photon-exciton, photon-phonon, photon-electron, photon-magneton, etc.) in solid matter is seen as one of the principal scientific concerns in the condensed matter discipline [1–5]. Modulating shorter pulse widths in laser perturbation strategies such as ultrafast spectroscopy, ultrafast electron, and x-ray diffraction techniques provides a good update to our comprehension of electron and phonon dynamics in photoexcited materials, with easily obtainable temporal resolutions on the tens of femtoseconds scale [6–9]. Ultrashort laser pulses are capable of generating far-from-equilibrium energy distributions with respect to degrees of freedom, leading to the detection of invisible orders that are not accessible in thermal equilibrium for many purposes, such as photoinduced superconductivity [10,11], charge-density waves [12,13], and ferroelectric-ferromagnetic phases [14,15]. Many of these processes can be described as transient corrections to the free energy landscape elicited by the redistribution of the quasiparticle population, dynamical corrections to the coupling strengths, and resonance-driven dynamics of the lattice. Ultrafast electron and x-ray diffraction show sensitivity to atomic-scale and femtosecond time-resolved structures, allowing averaged measurements over many unit cells [16–18], whereas time-domain theoretical schemes for lasers are capable of providing microscopic insights into the order-to-disorder phases engineered in ultrafast experiments for a deeper comprehension of photoinduced quantum states [19–24].

Chalcogenide phase-change materials (PCMs) are designated as candidates for all-optical integrated memory, where distinct resistive states and optical reflectivity contrasts resulting from laser pulses or electrical heating are mandatory for encoding in the phase-change memory process [25–28]. Of these, the most prototypical PCMs belong to the pseudobinary line of GeTe and Sb_2Te_3, $Ge_2Sb_2Te_5$ (GST-225), inherently IV–VI compounds, whose electronic structure is featured by the alignment of p-type bonds in the crystalline state [29–32]. Photodoping of p-type bonds involves two mutually coherent intrinsic stabilization mechanisms—resonant bond electronic dissipation and Peierls suppression distortion—whereas the physical origin of this steered ordered-disordered phase transition is currently the focus of a fascinating debate. Li *et al.* pioneered the removal of electrons from the high valence band state into a uniformly distributed electron gas background, enacting the GST-225 solid-solid amorphous phase transition [33]. Waldecker *et al.* observed a 30% shrinkage of the dielectric constant within 100 fs from ultrafast spectroscopy, without disturbing the crystalline order of GST-225 [34]. Until recently, Qi *et al.* verified the ultrafast laser-controlled localized structural change of the GST-225 unit cell from rhombohedral to cubic geometry within 0.3 ps. Experimentally, they screened the ultrafast diffraction information of localized structures using ultrafast electron diffraction probes, and observed the intensity decay with laser fluence in the time domain. Moreover, they described theoretical aspects of excited states by locking in the electronic population, stating the coherent phonon-mediated structural transient response
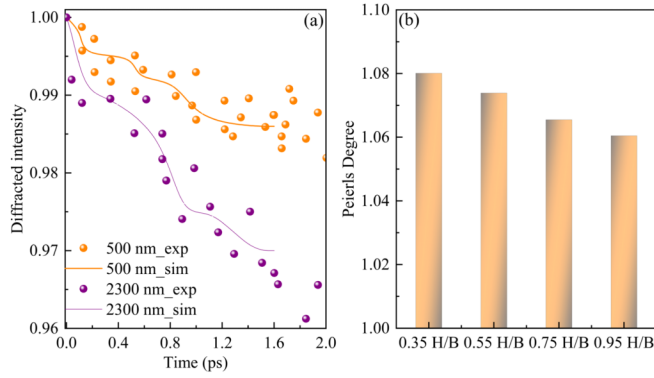

FIG. 1. Laser-illuminated microstructural characterization of GST-225. (a) rt-TDDFT simulation predicts the dynamic evolution of the diffracted intensity following valence electronic excitation, comparison of the simulated (solid line) with the experimental (dot line) data, at 500 nm and 2300 nm laser radiation, respectively. (b) The defined degree of Peierls distortion follows a range of laser external potentials. Here, the derived Peierls distortion is organized as the ratio of the long versus short bond lengths within a linear triatomic chain in the confined angle (∼180°).

[35]. Nevertheless, the transient occupation of electrons is incapable of time-dependent evolution of the photocarrier energy landscape, with speculative implications for the carrier relaxation dynamics during laser decoherence, as the electrons are constrained at the bottom of the conduction band at all times.

II. RESULTS

In this contribution, we employ real-time time-dependent density-functional theory (rt-TDDFT) to see the accurate repopulation landscape of photoexcited carriers in a prototype of GST-225, and restore the detailed equilibrium cooling process of extremely hot carriers via the introduced Boltzmann factor in all realistic ultrafast light-field illuminations (Appendix A). The metastable rocksalt GST-225 is commonly associated with bonding dynamics discrepancies dominated by Peierls distortion, i.e., an average distribution of long and short bonds organized in a localized structural motif. Such phenomena are rationalized by the half-filled electron-deficient *p* orbitals of resonance bonds. Depending on the defects and atomic proportions, one constructs an average rocksalt GST-225 lattice with anions fully occupied by Te atoms and cation sites randomly dominated by Ge (40%), Sb (40%), and vacancies (20%) based on the experimental data [36]. For the purpose of clarifying the physical mechanism of photoinduced phase transition, we first compare the diffraction findings of atomic dynamics upon ultrashort pulse excitation from two laser wavelengths according to ultrafast experiments [35]. Following the dynamical trajectory, with the initial lattice being in ambient equilibrium, we calculate the diffraction intensity [Fig. 1(a)] according to the Debye-Waller formula, $I(t) = \exp[-Q^2 \langle u^2(t) \rangle / 3]$, where Q is the vector of reciprocal lattices corresponding to the x-ray reflection peaks, and $\langle u^2(t) \rangle$ refers to the square of the root-mean-square displacement (RMSD) across all atoms (Appendix B, Fig. 5). The calculated data possess comparable agreement with the

experimental ones, which assists in backing up the reliability of the theoretical simulations.

Moreover, we track the dynamical picture of linear triatomic chains (Te-Ge-Te, Te-Sb-Te) at the same wavelength laser with different electronic excitations by tuning the laser external field, as shown in Fig. 1(b). Herein, the degree of Peierls distortion (Appendix C, Fig. 6) is specified as the linear angle (∼180°) of triatomic bonding, where any long and short bonds collected are divided equally, i.e., $\sum \bar{x}_i / \sum \bar{x}_j$, where x_i and x_j refer to long and short bond length, respectively. As the ratio gets close to 1, the localized Peierls distortion is attenuated, and vice versa, enhanced. One finds that the local structural motifs manifest ultrafast coherent Peierls-suppressed motions, and the degree of suppression is rather dependent on the electronic excitation. It follows that the laser wavelength resource and its varying laser fluence exert a dominant role on the dynamical behavior of photodoped GST-225.

III. DISCUSSION

We employ rt-TDDFT of the linear Hamiltonian implemented in the code PWmat [37–40] to mimic a real ultrafast laser, which is represented by the outer laser electric field combined with the Gaussian shape: $E_t = E_o \cos(\omega t) \exp[-(t - t_o)^2 / (2\sigma^2)]$ [41–46], where E_o is the amplitude of the electric field, $t_o = 60$ fs, the pulse width, $\sqrt{2}\sigma = 35$ fs, and the photon energy $\hbar\omega = 2.48$, 1.55 eV denote the 500 nm and 800 nm optically pumped pulses utilized in the experiment [34,35], respectively. Depending on the 500 nm laser tuned $E_o = 0.35$, 0.55, 0.75, 0.95 hartrees/bohr, the valence electrons are vertically excited on the order of about 1.86%, 4.13%, 6.78%, and 9.39% over a duration of 200 fs, as shown in Fig. 2(a). The calculation of the photocarrier in reciprocal space shows that short-pulse laser pumping enables deep excitation extending from the Fermi surface to the valence energy level, followed by repopulation to reside in an energy landscape with a broader conduction band, where the laser amplitude E_o ranges from 0.35 to 0.95 hartrees/bohr [Figs. 2(b)–2(e)]. The calculation of real space [Fig. 2(f)] further specifies the photoelectron distribution. These electrons are generated in a polarized distribution always on one side of the atom, the reason being that the average rocksalt GST-225 lattice suffers from localized Peierls distortions, whereas the A_{1g} phonon oscillations trap the atomic force to suppress the distortion along the ⟨111⟩ directions. In the photoexcitation event, the electron polarization releases the coherent force of the inverse A_{1g} motion, and the initial motion resonates with the A_{1g} phonon, the force of which is amplified as the external field increases. Moreover, these atomic forces operating on the heteropolar bonds diminish as the photoelectron and photogenerated hole pairs sustain recombination (Appendix C, Fig. 7). In combination with the evaluation of the constrained-occupation DFT [22,47], these inconsistent motions are attributable to the asymmetric morphing of the potential energy surface (PES) (Appendix D, Fig. 8) upon excitation of various phonon modes.

To examine the role of coherent versus thermal motion upon excitation, one can consider the fast Fourier transforms (FFT) of the localized Ge-Te bond lengths at temperatures
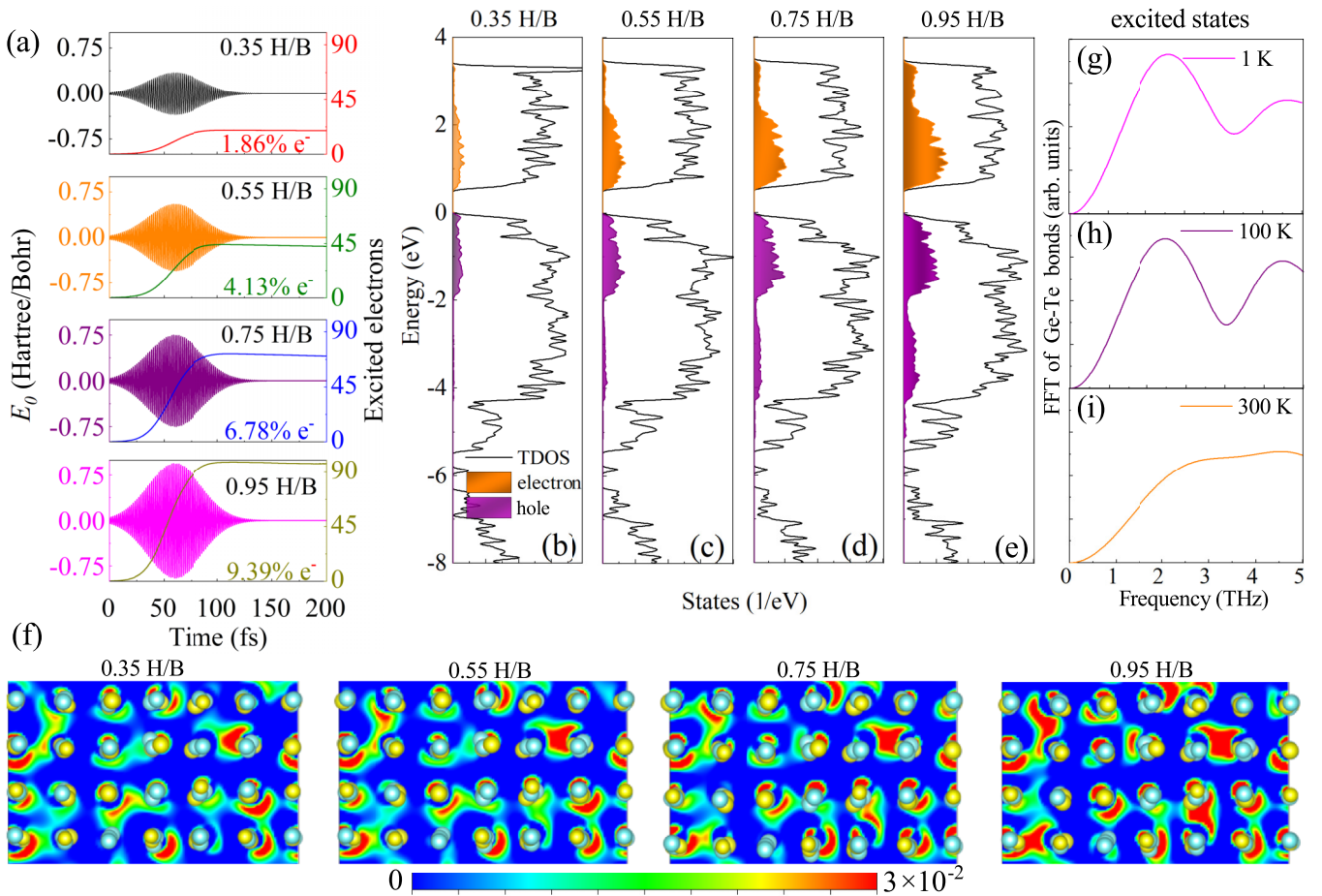
FIG. 2. Insights into real and reciprocal space for photoexcited carriers. (a) The shape of the external electric field applied to the GST, with laser intensity $E_o = 0.35$ to 0.95 hartrees/bohr. The number of excited electrons and the percentage depend on the laser pulse during the photoexcitation from the valence band to the conduction band. (b)–(e) Distributions of photoelectrons (shaded in orange) and photogenerated holes (shaded in violet) excited in the corresponding laser external field for a laser duration of 100 fs. (f) The real-space distribution of photoexcited electrons to empty bands above the Fermi level at the end of the laser pulse ($\sim$120 fs), modulated by each laser amplitude (0.35–0.95 hartrees/bohr). The photocarrier density maps allow for calculations following ρ(excited state) $-$ ρ(ground state). (g)–(i) Comparison of fast Fourier transforms of temperature-dependent localized Ge-Te bond lengths over time evolution with consistent laser amplitude. Here, we perform thermal equilibrium molecular dynamics for 3 ps at the corresponding temperatures (1 K, 100 K, 300 K) for the fully relaxed structures according to the *NVE* ensemble scheme, with the resulting structures serving as inputs to rt-TDDFT afterward.

of 1, 100, and 300 K upon consistent electronic excitation states, as shown in Figs. 2(g)–2(i). It can be seen that, at very low temperature, FFT signals consist of a single broad feature [Fig. 2(g)], while at 100 K and 300 K, the strength gradually weakens and transforms into double peaks [Fig. 2(h)] till it shifts from a ridgelike shape to a flat slopelike one [Fig. 2(i)]. Instead, when we turn to consider the lattice temperature consistency, it seems clear that the increased electronic excitation contributes to a consistent reinforcement of the local coherent motion amplitude (Appendix D, Fig. 9). Hence, coherent phonons are expected to compete and associate with thermal phonons in triggering photoexcitation.

The crystal orbital Hamiltonian population (COHP) analysis allows for the quantitative measurement of bond strength in crystalline structure (by means of $-$COHP values), where positive and negative signs refer to bonding and antibonding states, respectively. Then, we analyze the COHP of the ground-state rocksalt GST-225, which, as evident from

Fig. 3(a), has a small distribution of antibonding states in the shallow (-2 to 0 eV) region of the valence band, derived either from Ge-Te or Sb-Te bonds. We observe in both theoretical modeling and electron diffraction experiments [Fig. 1(a)] that the diffraction decay at 2300 nm (visible to the naked eye) is faster than that at 500 nm for almost the same amount of valence electron excitation depending on the extrapolation of the electron-hole plasma density (Appendix B), which motivates us to explore the lattice disorder in the photoinduced amorphization of GST via employing different laser resources, albeit keeping the same electronic excitation ratio. Accordingly, one explores the state distributions of photoelectrons and photogenerated holes at the same electronic excitations ($\sim$9% of the outer valence electrons) of 500 nm [Fig. 3(b)] and 800 nm [Fig. 3(c)]. We stress that the 800 nm femtosecond laser has been used rationally in the GST nonthermal phase transition during photoinduced amorphization and is an available laser resource for GST ultrafast experiments [34].
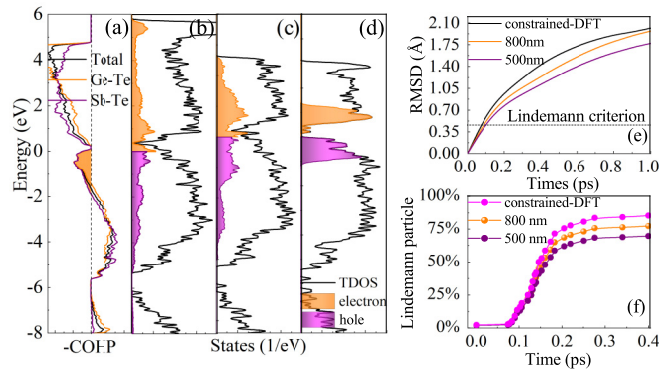
FIG. 3. Photoexcited amorphization of rocksalt GST-225. (a) The −COHP plot of the average value of Ge-Te and Sb-Te bond interactions. (b)–(d) Distribution of photoexcited electrons and holes at the same high electronic excitation content by 500, 800 nm pulsed laser as well as by manually excited case. The manual scheme means that the electrons at the top of the valence band are mechanically moved to occupy the bottom of the conduction band in the same proportion as the pulsed optical excitation. These electrons are fixed at the bottom of the conduction band without participating in time-domain evolution of the hot-carrier cooling process. (e) Simulation-predicted atomic RMSD as a function of time upon photoexcitation. The dashed line represents the Lindemann criterion, i.e., $r_c = 0.45$ Å [15% of the average rocksalt GST-225 (3 Å)]. (f) Percentage of Lindemann particles produced over time for intense excitation at 500 nm (0.95 hartrees/bohr), 800 nm (1.30 hartrees/bohr) ultrafast lasers and manual excitation. The growth rate of Lindemann particles occurs for the three strong excitations of interest as, manually excited faster, followed by 800 nm laser irradiation and relatively slower by 500 nm irradiation.

Moreover, about 9% of the valence electrons are needed to be excited to render the crystalline phase disordered, whereas the 2300 nm laser has a very small single-photon energy ($h\omega = 0.54$ eV) and a larger laser amplitude is needed for a strong excitation, which makes the computational process tough. This situation, however, can be solved by taking amplitude values of 0.95 hartrees/bohr and 1.30 hartrees/bohr at 500 nm and 800 nm wavelengths, respectively, to achieve the same percentage of electronic excitation (Appendix E, Fig. 10). One can see that the short-wavelength excitation possesses a wide hot-carrier energy range as compared to the long-wavelength one, provided that both photon energies are above energy gap, whereas the latter prefers to pump more centrally the antibonding electrons in the Fermi surface over the former, which is eventually reflected as a saturated excitation of the photogenerated hole numbers (Appendix E, Fig. 11). Further, we employ a manual excitation scheme [33] to consider the electronic excitation scenario on the limit. One can see that the manual excitation maps out a more localized landscape of photoinduced electrons and holes, with this supposedly generating atomic driving forces to stretch the nonhomopolar bonds, lowering the free energy of the excited system. Intense excitation evidences a reserve of sufficient momentum [Fig. 2(f)] as well as a lower barrier (Appendix D, Fig. 8) implying the beginning of the photoinduced glassy state.

Regarding solids, the Lindemann criterion says that crystals liquify as the amplitude of the atomic thermal vibrations

exceeds 15% of interatomic spacing [48,49]. We record the root-mean-square displacements with so-called Lindemann particles as a criterion for labeling the appearance of molten particles. Here, on the premise of including electronic excitation consistent with the manual scheme, one can observe that the longer pulsed lasers steer the long-range disordering process faster as the earliest Lindemann criterion is reached and the fastest expansion of its atomic diffusion displacement is achieved, as shown in Fig. 3(e). Moreover, the growth of such Lindemann particles on finer timescales, as shown in Fig. 3(f), manifests itself in a nucleation-like disordered state of atomic clusters in three excitations (500 nm, 800 nm, and the manual scheme). Evidently, the dynamics of the phase transition induced in the nonthermal channel is distinct from the homogeneous melting mechanism of the thermally induced phase transition. Hence, ultrafast dissipation of electrons from the antibonding states of resonance bonds greatly contributes to photoamorphization.

The dominant procedure is carrier relaxation to lower energy states within the conduction band provided that the excited electrons mainly occupy the higher energy states [50]. Description of the cooling of extremely hot carriers is infrequently a theoretical exercise, as most of the rt-TDDFT simulations are able to describe only the instantaneous dynamics of the excited system following photoexcitation [51,52]. In our concern, we introduce a Boltzmann factor τ for including hot-carrier cooling effects, which restores the detailed balance with respect to the various electronic state transitions and thus correctly treats the cooling events. Figures 4(a)–4(e) show the dynamic evolution of excited electrons and holes upon 500 nm pulsed laser excitation over the longer times considered. One can see that the excited hot electrons occur in band nonradiative recombination over a duration of 300 to 1800 fs, a multilevel carrier dynamical process. Considering the energy conversion perspective, atomic potential energy follows the total energy during the initial excitation of 120 fs showing a simultaneous elevated Gaussian envelope evolution, as depicted in the inset miniplot of Fig. 4(f). The atomic kinetic energy stays low during this period, indicative of electron-electron interplays rather than phonon-assisted processes, a reminiscence of the incomplete attainment of the Lindemann criterion for the lattice.

A simultaneous increment in atomic kinetic energy accompanies the energy transfer from hot-carrier cooling to the lattice subsystem. The higher the photocarrier density, the quicker the induced modulation of the electronic structure, thereby contributing to the electron-phonon coupling for stronger phonon excitations. It can reshape PES, allowing metallization and elimination of crystalline memory in a timescale comparable to that of purely electronic processes. We follow the evolution of Lindemann particles during the cooling of hot carriers. A comprehensive search of several dynamical trajectories of the evolution shows that the molten particles are randomly distributed inside the lattice, as shown in Fig. 4(g). Following the hot-carrier cooling, these Lindemann particles connect neighboring networks to form distorted atomic groups, contributing to the ultrafast formation of the chalcogenide glassy state. Differing from the potential-induced "rattling" model [53], orbital-selective
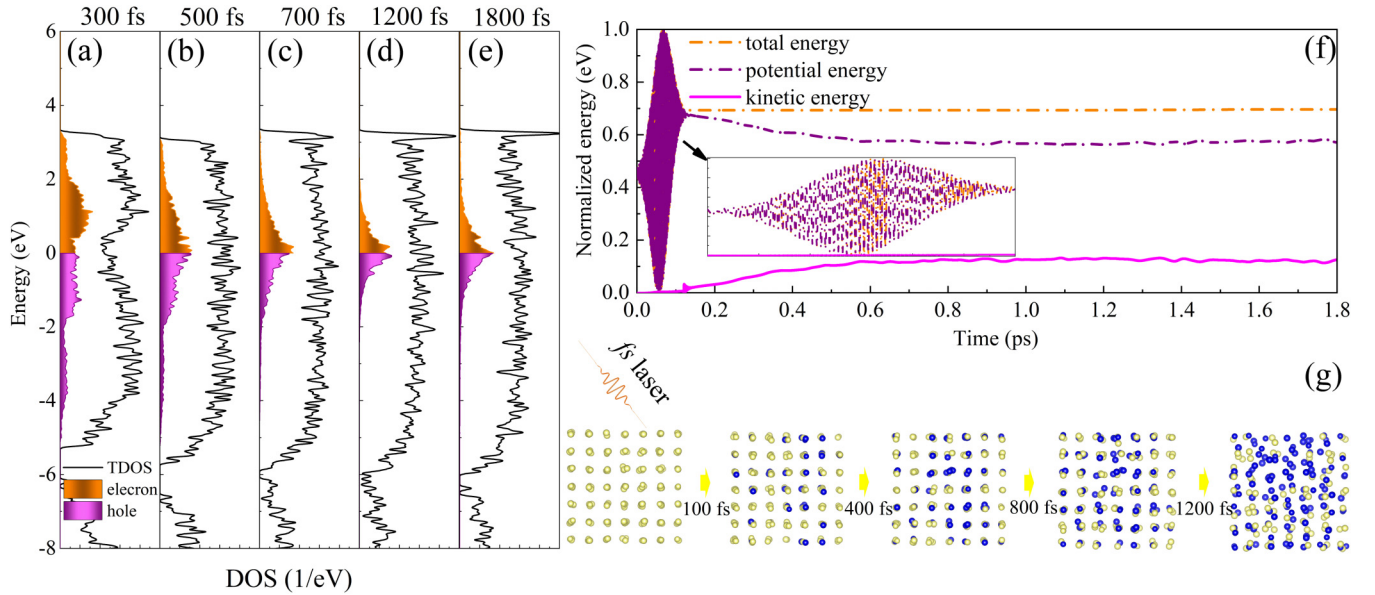
FIG. 4. Photoexcited hot-carrier cooling event in rocksalt GST-225. (a)–(e) Nonradiative recombination landscape of photoexcited electrons and photogenerated holes in tracked dynamical trajectories. (f) Regarding the total energy, potential energy, and dynamic energy conversion images of the system following photoexcitation over a longer period of time as the hot carriers cool. (g) Snapshots of atomic displacements observed along the [001] direction at 100, 400, 800, and 1200 fs after photoexcitation. The Lindemann particles with activity radii exceeding 0.45 Å are color-coded in blue.

hopping of electrons [54], carrier multiplication [50], and thermally induced phase transitions [55], ultrafast dissipation of antibonded electrons establishes a dynamical coupling with the phase engineering of ordered to disordered nonequilibrium states.

IV. CONCLUSIONS

In summary, we investigate the multilevel optical excitation dynamics of the rocksalt GST-225 lattice intertwined with nonequilibrium states using state-of-the-art time-dependent density-functional theory. Without any *a priori* hypothesis, we reproduce the diffraction data from 500 nm and 2300 nm short-pulse lasers with the respective fluences. Locally microscopic A_{1g} coherence forces suppress the coherent Peierls distortion ultrafast upon laser amplitude elevation. Following the scenario, we focus on the strong dependence of the photoinduced amorphization process upon the same electronic excitation subjected to changing laser wavelengths, with longer-wavelength lasers leading to localized volumes catering to the Lindemann criterion faster as compared to shorter-wavelength ones. The extreme hot-carrier cooling is followed by the nonradiative recombination of photoelectrons with photogenerated holes, and atomic energy conversion expresses a switch from purely electronic processes to electron-phonon interactions, in which localized Lindemann displacements disturb the crystalline order of the neighboring network. We anticipate that this work serves as a guiding principle in locating other photoinduced states by identifying the general character of the Peierls distortion with the loss of resonance bonds, connecting between equilibrium fluctuations and out-of-equilibrium ordering.

APPENDIX A: THEORETICAL APPROACH TO THE rt-TDDFT OF THE LINEAR HAMILTONIAN WITH BOLTZMANN FACTOR

We perform the *ab-initio*-MD and rt-TDDFT simulations based on the norm-conserving pseudopotentials and PBE exchange-correlation functional, which is implemented in the code PWmat. In the rt-TDDFT simulations, we employ a 194-atom supercell containing 43 germanium, 43 antimony, and 108 tellurium atoms for GST-225 with Brillouin zone integrations at the Γ point. The plane-wave energy cutoff is 50 Ry. The coupling among the atomic and electronic motions is modulated by the Ehrenfest approximation. The time step we adopt for the rt-TDDFT simulation (0.1 fs) is much larger than that of the conventional TDDFT (subattosecond) [56–59].

In the case of rt-TDDFT MD, the time-dependent Kohn-Sham single-particle equation is

$$i\frac{\partial \psi_i(t)}{\partial t} = H[\rho(t)]\psi_i(t), \tag{A1}$$

where $\psi_i(t)$ refers to the time-dependent single-particle wave function of index i, with $\rho(t)$ being the time-dependent charge density. $\rho(t)$ is available from $\psi_i(t)$ and then

$$\rho(t) = \sum_i O_i(t)|\psi_i(t)|^2, \tag{A2}$$

in which $O_i(t)$ is the occupancy of electrons on state $\psi_i(t)$. The ionic positions $R_k(t)$ (k represents the atom index) are taken into account by the Hamiltonian equation via the Coulombic interaction from the nucleus to the electrons, whereas the motion of $R_k(t)$ is generalized via Newton's second law using the *ab initio* force $F_k(t)$ and the ionic mass

$$\frac{M_k(t)d^2R_k(t)}{dt^2} = F_k(t)/M_k(t). \tag{A3}$$

The instantaneous approximation given by the TDDFT method is conditioned on the fact that $H[\rho(t)]$ follows the traditional interpretation of the exchange-correlation function. The solution of Eq. (A1) is commonly integrated by the formula $\psi_j(t + \Delta t) = \exp[(-iH\Delta t)\psi_j(t)]$, for which a time step Δt is desired that satisfies $|H\Delta t|$, yielding an effective $\Delta t \leqslant 1$ as (since the Hamiltonian energy spectrum of the plane-wave basis set is typically larger than 10^2 eV).

To tackle the bilateral challenges of high time step count and heavy computational cost imposed by the traditional rt-TDDFT algorithm, the time-dependent wave function $\psi_i(t)$ is developed into an adiabatic eigenstate $\phi_i(t)$ that simplifies favorably in time,

$$\psi_i(t) = \sum_l C_{i,l}(t)\phi_l(t), \tag{A4}$$

$$H(t)\phi_l(t) \equiv \epsilon_i(t)\phi_l(t), \tag{A5}$$

where $H(t) \equiv H(t, R(t), \rho(t))$; $\rho(t)$ and $R(t)$ represent the charge density and the nuclear position, respectively. Combining Eqs. (A4) and (A5) followed by substitution into Eq. (A1) leads to

$$ih\frac{\partial}{\partial t}\dot{C}_{i,l}(t) = \sum_j [C_{i,j}(t)H_{l,j}(t)]. \tag{A6}$$

In Eq. (A6), the Hamiltonian $H(t)$ at t_1 and t_2 can be expressed as a linear relationship over time. To refine, as regards a time interval $[t_1, t_1 + \Delta t]$, the eigenstates at t_1 $[\psi_l(t_1)]$ are treated as extensions to the basis set of the Hamiltonian equation. Instead of the Hamiltonian at t_1 containing the diagonal term $\{\epsilon_1(t_1)\}$, it is diagonal at the basis set $\{\psi_l(t_1 + \Delta t)$ of $t_1 + \Delta t$. one can assume that the Hamiltonian acts in a linear fashion on $[t_1, t_2]$. For any $t \in [t_1, t_2]$,

$$H(t) = H(t_1) + \frac{(t - t_1)}{\Delta t}[H(t_1 + \Delta t) - H(t_1)]. \tag{A7}$$

In the adiabatic eigenstate basis set, the linear approximation of the Hamiltonian then serves as a good flavor of the real $H(t)$ ($\Delta t \leqslant 0.2$ fs), which is several orders of magnitude longer than the time step 1 as in the conventional rt-TDDFT. Trying to solve Eq. (A6) within $[t_1, t_1 + \Delta t]$ involves integrating in multiple steps with smaller d_t in $[t_1, t_1 + \Delta t]$ (here, $d_t = 10^{-1}$ to 10^0 as). Notably, rather than solving $\{\phi_l(t), \epsilon_l(t)\}$ directly from $H(t)\phi_l(t) \equiv \epsilon_i(t)\phi_l(t)$, one generates $H(t)$ according to Eq. (A7), followed by diagonalizing it under a

small basis set of $\{\phi_l t_1\}$. The production and diagonalization of the $M \times M$ matrix $H(t)$ (M refers to the number of adiabatic states) consumes only a short time [Eq. (A7)].

To overcome the imbalance of the original rt-TDDFT evolution in describing the hot-carrier cooling process, the adiabatic states are used to extend the wave function. Specifically, the charge flow correlation between adiabatic states i and i' first needs to be determined. which is described as follows:

$$T(i, i', t) = -2\sum_{j=1}^N \text{Re}\{iC_{j,i}^*(t)V_{i,i'}(t)C_{j,i'}(t)\}. \tag{A8}$$

Here, $C_{j,i}$ refers to the wave function expansion coefficients. The charge flow comes from all wave functions $\psi_j(t)$ instead of any of them. $T(i, i', t)$ represents the charge flow from the adiabatic state i' to the adiabatic state i. $T(i, i', t)$ is constant under the unitary rotation of the subspace to which $\psi_j(t)$ belongs, and there is $T(i, i', t) = -T(i, i', t)$. Regarding the decoherence effect, it is necessary to define the time-averaged $T(i, i', t)$ as

$$I(i, i', t) = \frac{1}{\tau_{i,i'}}\int_0^\infty T(i, i', t - t')e^{-\frac{t'}{\tau_{i,i'}}}dt'. \tag{A9}$$

Here, $\tau_{i,i'}$ refers to the decoherence time between adiabatic states i and i'. We need to modify the time-evolution equation to deal with the imbalance defect; i.e., the average charge flow from i' to i is changed according to the detailed equilibrium. We then modify $I(i, i', t)$ to include a $\Delta I(i, i', t)$ as follows:

$$\Delta I = \begin{cases} I(i, i', t)\left(e^{-\frac{|\epsilon_i - \epsilon_i'|}{KT}} - 1\right), & I(i, i', t)(\epsilon_i - \epsilon_i') > 0, \\ 0, & I(i, i', t)(\epsilon_i - \epsilon_i') \leqslant 0. \end{cases} \tag{A10}$$

Here, ϵ_i, $\epsilon_{i'}$ denote the adiabatic eigenstates and T is the temperature. Therefore, $\Delta I(i, i', t)$ is actually a modification to the charge flow $T(i, i', t)$. This modification is realized by adding a $\Delta C_{j,i}(t)$ after each step of the wave function evolution from t_1 to $t_1 + \Delta t$, i.e., by altering the wave function $C_{j,i}(t)$,

$$\sum_{i=1}^M C_{j_1,i}(t)\Delta C_{j_2,i}^*(t) + \Delta C_{j_1,i}(t)\Delta C_{j_2,i}^*(t) = 0, \tag{A11}$$

$$2\sum_{j=1}^N \text{Re}[C_{j,i}(t)\Delta C_{j,i}^*(t)] = \Delta t\sum_{i'}\Delta I(i, i', t). \tag{A12}$$

The above two equations are used to satisfy the orthogonality condition for $\psi_j(t)$ and to tailor the occupation of the adiabatic state by introducing $\Delta I(i, i', t)$, respectively, and both are solved by the conjugate gradient method. The optimal solution is the one that is needed to find the minimum amplitude $\Delta C_{j,i}(t)$ solution that satisfies the above equations. Energy is not conserved by introducing $\Delta C_{j,i}(t)$. By subtracting the velocities of the transition degrees of freedom, energy conservation is being restored with the formula $\Delta I(i, i', t)$. Concerning hot-carrier cooling and energy transfer, $\Delta I(i, i', t)$ provides an explanation for the total energy change. It can be used to determine a transition degree of freedom (TDF)
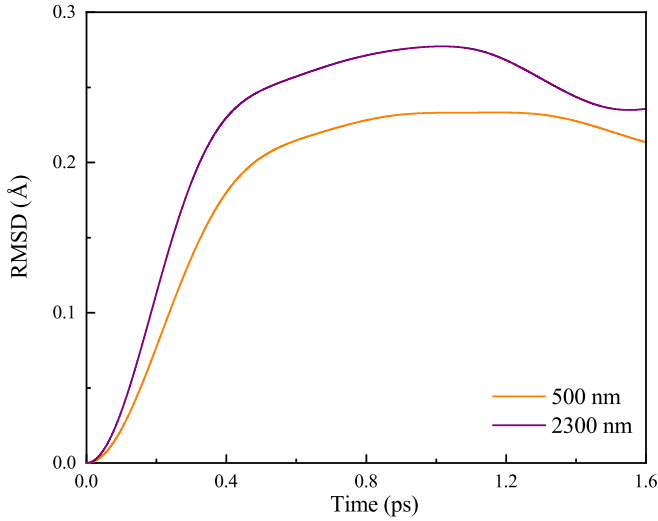
FIG. 5. Mean root-mean-square displacements (RMSDs) of rocksalt GST following photoexcitation at comparable laser fluences of 500 nm and 2300 nm.

manifested by a set of atomic forces:

$$F_{\text{TDF}}(R_a, t) = \sum_{i,i'} \Delta I(i, i', t)/|d(i, i', t)|,$$

$$\text{Re}\left\{ \langle \phi'_i(t)| \frac{\partial H(t)}{\partial R_a} |\phi_i(t)\rangle d(i, i', t) \right\}. \quad \text{(A13)}$$

Here R_a refers to atomic occupation of atom a; $d(i, i', t) = \sum_{j=1}^{N} C(i, j, t)C^*(i, j, t)$ is employed to tune the appropriate phases for the $\phi_i(t)$ and $\phi_{i'}(t)$ terms. To be explicit, one is able to evaluate the total energy $E_{\text{DFT}}[\psi(t)]$ and then the total energy change $\Delta E = E_{\text{tot}} - E_{\text{DFT}} - E_{\text{kin}}$. Here, E_{kin} and E_{tot} are, respectively, the nuclear kinetic energy as well as the initial conserved total energy. We then rescale the velocity from

$$V'(R_a, t) = V(R_a, t) + aF_{\text{TDF}}(R_a, t)/M_a. \quad \text{(A14)}$$

In this case, M_a is the nuclear mass and the coefficient α is determined to allow the kinetic energy to increase by ΔE. Being that ΔE is commonly positive (the impact of the Boltzmann factor is always to lower the total energy; one never finds the opposite), it follows that the conservation of energy can always be satisfied. By subtracting the velocities of the transition degrees of freedom, energy conservation is being restored with the formula $\Delta I(i, i', t)$. When adding this factor, however, the decoherence time τ (in fs) for the transition between all adiabatic states should be taken into account; otherwise the cooling speed could be too fast. In our considerations for the supercell GST-225, we use a uniform $\tau_{i,i'} = 20$ fs to denote this effect, since $\tau_{i,i'}$ is typically in this range for a variety of different systems [60–62], which ensures that there are no large amplitudes $\Delta C_{j,i}(t)$ between adiabatic states, favoring the convergence of the TDDFT algorithm as well as the detailed equilibrium of the cooling process.

APPENDIX B: ROOT-MEAN-SQUARE DISPLACEMENT

The electron-hole plasma density developed by a prototypical subpicosecond laser pulse is given by $N_{e-h} \approx$
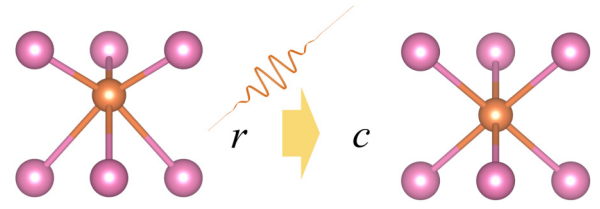

FIG. 6. Coherent motion of localized rhombic-to-cubic geometry upon intense laser illumination.

$(1 - R)\alpha_{eff}F/h\omega$, where F and ω represent the intensity and frequency of the pulsed laser, with R and α_{eff} corresponding to the reflectivity and linear absorption coefficient of the metastable phase, respectively [63]. For the 2300 nm laser, $h\omega = 0.54$ eV, $R = 0.6$, and $\alpha_{eff} = 2 \times 10^4$ cm^{-1} [64,65]. For the 500 nm laser excitation, $h\omega = 2.48$ eV, $R = 0.74$, and $\alpha_{eff} = 1 \times 10^6$ cm^{-15} [65–67]. For a GST sample of experimentally given thickness ($l = 15$ nm), the absorbed optical energy density is $N_{e-h} \approx (1 - T)F/h\omega$, where $T = I/I_0 = \exp(-\alpha_{eff}l)$. For 15 nm thick GST-225, $T_{2300} = 0.97$ and $T_{500} = 0.22$. The total number of valence electrons in rocksalt GST-225 is $N_e(\text{total}) = 1.76 \times 10^{23}$ cm^{-3} [68]; then the corresponding total number within 15 nm is 2.64×10^{17} cm^{-2}. Also, the experimental pump fluences of 2300 nm and 500 nm lasers are about 2–7 mJ/cm^2 and 0.3–0.8 mJ/cm^2, which yield $N_{e-h}(2300) \approx (0.69$–$2.43) \times 10^{15}$ cm^{-2} and $N_{e-h}(500) \approx (0.59$–$1.57) \times 10^{15}$ cm^{-2} [35].

In our rt-TDDFT simulations, we apply a time-dependent external electric field in a Gaussian shape, $E_t = E_o \cos(\omega t) \exp[-(t - t_o)^2/(2\sigma^2)]$, where we choose photon energy $h\omega = 2.48$ eV, $t_o = 60$ fs, and $\sqrt{2}\sigma = 35$ fs, and four laser fluences $E_o = 0.35$, 0.55, 0.75, and 0.95 hartrees/bohr (or 0.1801, 0.2831, 0.386, and 0.4889 V/Å). Our electric field polarization is along the x, y, and z directions. In real space, the external electric field is modeled using a zigzag inhomogeneous potential, e.g., with the linear functions $V_{\text{ext}}(r) = (x - 0.5) + (y - 0.5) + (z - 0.5)$ and $H(t) = H_0 + V_{\text{ext}}(r)E(t)$. We further unify all the units of the electric field and calculate the total laser fluence in the unit of W/cm^2, which is of course the laser energy per second passing through a given surface area. Thus, the original laser electric field values 0.35, 0.55, 0.75, and 0.95 hartrees/bohr can be converted
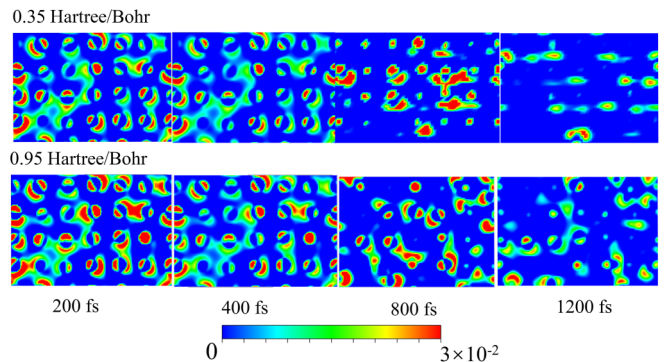

FIG. 7. Real-space distributions of photoelectron and photogenerated hole pairs regulated by two laser amplitudes of interest (0.35, 0.95 hartrees/bohr) as a function of time.
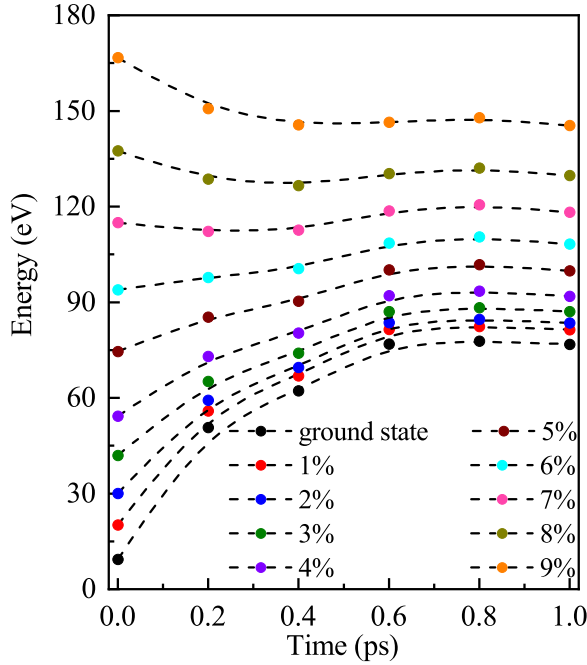
FIG. 8. Photoexcitation modified PESs under laser pulses with different electronic excitations.
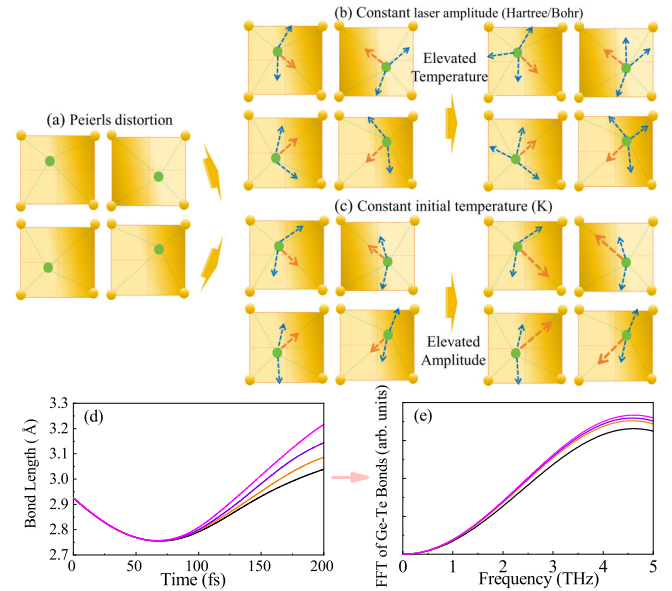

FIG. 9. (a) Rocksalt lattice of Peierls distortion under thermal equilibrium conditions. (b) Atomic displacements from elevated lattice temperatures under constant laser amplitude condition. The orange and green arrows refer to microscopic coherent and thermally disordered motions, respectively. (c) Atomic displacements from continuously elevated laser amplitudes under constant initial lattice temperature. (d) Statistics over time of the local Ge-Te bond lengths for each laser amplitude modulation at ambient temperature, followed by fast Fourier transforms to the bond lengths (e), respectively.

to 0.43, 1.06, 1.98, and 3.17×10^{12} W/cm^2. Nevertheless, since there are some uncertainties in the absolute laser field strength (localized optical absorption and reflection) and periodic boundary conditions, the total electronic excitation is a more robust match to the experimental data. Then, according to the laser fluences of 4.6 mJ/cm^2 and 0.61 mJ/cm^2 obtained in the experimental 500 nm and 2300 nm wavelengths, it is estimated that the percentage of the outermost excited electrons accounts for 0.61% and 0.45%, respectively, which are comparable. We then tailor the laser amplitude E_o so as to excite the number of electrons in each of the above two percentages, and obtain the root-mean-square displacements (RMSDs) through the dynamical trajectories, as shown in Fig. 5.

APPENDIX C: DEGREE OF PEIERLS DISTORTION AND RECOMBINATION OF PHOTOELECTRONS WITH PHOTOGENERATED HOLES

Peierls distortion is typically found in crystalline PCMs and other semiconductors: such symmetry-lowering distortion leads to the formation of long and short bonding pairs and a widening of the band gap. In the amorphous phase, Peierls-like distortions can be quantified by calculating the bond distribution over bonding pairs with an angle close to 180° [69]. Here, to quantify the bond length distribution and Peierls distortion within 200 fs of initial excitation in the TDDFT-MD process, a sample of 200 uniformly distributed structures from that period are considered. In practice, the bond pair characterizing the Peierls distortion is identified as two linearly aligned bonds with angles deviating from 180° by less than 30°. As shown in Fig. 6, intense laser radiation produces an ultrafast localized response in rhombic to cubic

geometries, as reminiscent of the weakening of the degree of Peierls distortion in a unitary structural motif.

We picture the distribution of photoelectrons in real space over longer times when the cooling term is included, for the minimum (0.35 hartrees/bohr) and maximum (0.95 hartrees/bohr) laser amplitudes considered in the photoexcitation event, respectively, as shown in Fig. 7. In reality, hot carriers tend to relax to lower-energy electronic states and transfer the released energy to the lattice via electron-phonon interactions, applicable to both the smaller localized A_{1g} coherence force (0.35 hartrees/bohr) and the larger one (0.95 hartrees/bohr) at the very beginning moment (200 fs). These atomic forces operating on the heteropolar bonds,
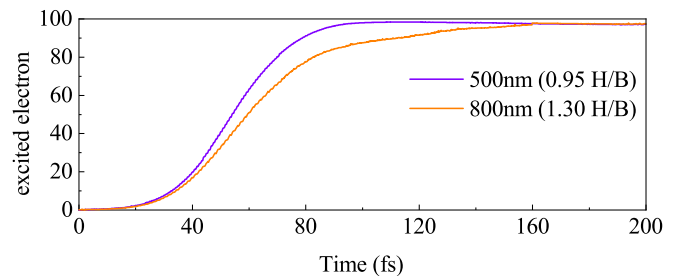

FIG. 10. The ultrafast lasers at 500 nm and 800 nm wavelength resources are included to produce equal amounts of electronic excitation (about 9% of the outermost electrons) using laser amplitudes moderated by 0.95 hartrees/bohr and 1.30 hartrees/bohr, respectively.
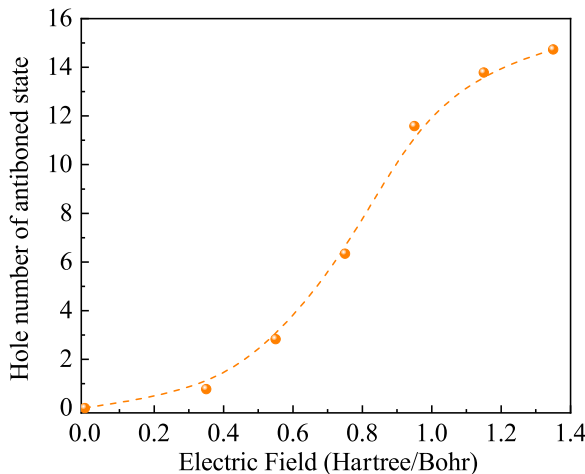
FIG. 11. The number of excited holes on the Fermi surface of the antibonded state at growing 500 nm laser amplitude.

however, are released with the process of sustained recombination of photoelectron and photogenerated hole pairs, collaborating with the lattice to perform stable thermal motions as well as photoinduced amorphization. We believe that electron-phonon equilibration time is mainly due to the equilibration process of lattice thermal motions following the initial coherent motions with atomic kinetic energy obtained from the carrier cooling.

APPENDIX D: POTENTIAL ENERGY SURFACE AND FAST FOURIER TRANSFORMS

To evaluate the atomic dynamics mediated by the laser external field, we examined the corresponding photoexcited modified PESs at various laser intensities according to the occupancy-constrained DFT calculations, and the results are compared in Fig. 8. We find that photoexcitation elevates the potential of the ground state and relatively decreases the potential energy barrier for amorphization events as the intensity of electronic excitation increases. This leads to a slope of the photoexcitation modified PES curve from the ordered phase to the disordered phase. This slope provides an opportunity for the emergence of molten particles to reorder the crystalline phase.

In the case of thermal equilibrium based on the Born-Oppenheimer *ab initio* molecular dynamics, the rocksalt lattice develops Peierls distortion as shown in Fig. 9(a), which is locally correlated with the A_{1g} coherence in the structure. For the discussion of the FFT, we distinguish between the conditions of constant laser amplitude [Fig. 9(b)] and constant initial lattice temperature [Fig. 9(c)]. In Fig. 9(b), the elevated lattice temperatures contribute to the intensified thermal

motion of the atoms at the lattice sites, which is the force of the undirected thermal random motion against the coherent one. The temperature-dependent FFT data in Figs. 2(g)–2(i) are fast Fourier transforms of the sampled bond lengths over time. Therefore, the intensity of the coherence peak weakens with elevated temperature.

At a consistent lattice temperature [Fig. 9(c)], the temporally evolved localized Ge-Te bond-length statistics [Fig. 9(d)], followed by the fast Fourier transform of the bond length [Fig. 9(e)], show that the coherent motion is enhanced gradually with the increase of the laser amplitude, which is consistent with the distribution of photoelectrons in the real space. Here, the coherent and thermally disordered motions manifest clearly the contending levels of modulated lattice order. One can see that the coherence peak is elevated as the external potential gradually increases. That is, the elevated lattice temperature affects the initial atomic order and is indicative of disordered states, whereas the enhancement of the external potential is capable of amplifying the localized coherent motion.

APPENDIX E: PHOTOINDUCED AMORPHIZATION AND PHOTOGENERATED ANTIBONDED HOLE NUMBER NEAR FERMI SURFACE

Intense electronic excitation is shown to produce ultrafast nonthermal melting of chalcogenide phase-change materials [33], as well as other families, in known cases [70]. Therefore, we employ a consistent amount of electronic excitation (about 9% of valence electrons) at two different wavelengths of modulation (500 nm, 800 nm), demanding a laser amplitude of 0.95 hartrees/bohr (500 nm) as well as 1.30 hartrees/bohr (800 nm), respectively. As indicated in Fig. 10, long-wavelength lasers possess smaller single-photon energies than short-wavelength ones, so a larger laser amplitude is desired to modulate the excitation of equal electrons.

According to Fermi's golden rule, by which the density of photoexcited electrons allowed to transition from the valence band to the conduction band within individual time intervals scales proportionally to the density of (initial) electrons occupying the valence band and the density of (final) conduction-band empty states, the sufficient momentum resources are available from strong photon scattering. In cases where a substantial number of electrons are excited from the valence band to the conduction band, the densities of both the initial electrons and the final empty state are lowered considerably, yielding a sublinear dependence of the excited electrons (holes left behind) on the intensity of the laser illumination. As shown in Fig. 11, one counts the region of antibonding states near the Fermi surface occupying the negative orbital overlap, where the number of holes left behind by photoexcitation exhibits a saturated growth depending on the band-filling rule.

[1] M. X. Na, A. K. Mills, F. Boschini, M. Michiardi, B. Nosarzewski, R. P. Day, E. Razzoli, A. Sheyerman, M. Schneider, G. Levy, S. Zhdanovich, T. P. Devereaux, A. F. Kemper, D. J. Jones, and A. Damascelli, Direct determination of mode-projected electron-phonon coupling in the time domain, Science **366**, 1231 (2019).

[2] M. J. Stern, L. P. René de Cotret, M. R. Otto, R. P. Chatelain, J.-P. Boisvert, M. Sutton, and B. J. Siwick, Mapping momentum-dependent electron-phonon coupling and nonequilibrium phonon dynamics with ultrafast electron diffuse scattering, Phys. Rev. B **97**, 165416 (2018).

[3] O. Lee, K. Yamamoto, M. Umeda, C. W. Zollitsch, M. Elyasi, T. Kikkawa, E. Saitoh, G. E. W. Bauer, and H. Kurebayashi, Nonlinear magnon polaritons, Phys. Rev. Lett. **130**, 046703 (2023).

[4] M. Mitrano, A. Cantaluppi, D. Nicoletti, S. Kaiser, A. Perucchi, S. Lupi, P. Di Pietro, D. Pontiroli, M. Riccò, S. R. Clark, D. Jaksch, and A. Cavalleri, Possible light-induced superconductivity in K_3C_{60} at high temperature, Nature (London) **530**, 461 (2016).

[5] L. Waldecker, R. Bertoni, H. Hubener, T. Brumme, T. Vasileiadis, D. Zahn, A. Rubio, and R. Ernstorfer, Momentum-resolved view of electron-phonon coupling in multilayer WSe_2, Phys. Rev. Lett. **119**, 036803 (2017).

[6] Z. H. Loh, G. Doumy, C. Arnold, L. Kjellsson, S. H. Southworth, A. A. Haddad, Y. Kumagai, M. F. Tu, P. J. Ho, A. M. March, R. D. Schaller, M. S. Bin Mohd Yusof, T. Debnath, M. Simon, R. Welsch, L. Inhester, K. Khalili, K. Nanda, A. I. Krylov, S. Moeller *et al.*, Observation of the fastest chemical processes in the radiolysis of water, Science **367**, 179 (2020).

[7] C. W. Nicholson, A. Lucke, W. G. Schmidt, M. Puppin, L. Rettig, R. Ernstorfer, and M. Wolf, Beyond the molecular movie: Dynamics of bands and bonds during a photoinduced phase transition, Science **362**, 821 (2018).

[8] G. Jarc, S. Y. Mathengattil, A. Montanaro, F. Giusti, E. M. Rigoni, R. Sergo, F. Fassioli, S. Winnerl, S. D. Zilio, D. Mihailovic, P. Prelovšek, M. Eckstein, and D. Fausti, Cavity-mediated thermal control of metal-to-insulator transition in $1T$-TaS_2, Nature (London) **622**, 487 (2023).

[9] A. Sood, X. Z. Shen, Y. Shi, S. Kumar, S. J. Park, M. Zajac, Y. F. Sun, L. Q. Chen, S. Ramanathan, X. J. Wang, W. C. Chueh, and A. M. Lindenberg, Universal phase dynamics in VO_2 switches revealed by ultrafast operando diffraction, Science **373**, 352 (2021).

[10] K. A. Cremin, J. D. Zhang, C. C. Homes, G. D. Guc, Z. Y. Sun, M. M. Foglera, A. J. Millis, D. N. Basov, and R. D. Averitt, Photoenhanced metastable c-axis electrodynamics in stripe-ordered cuprate $LaS_{1.885}BaS_{0.115}CuOS_4$, Proc. Natl. Acad. Sci. USA **116**, 19875 (2019).

[11] M. Budden, T. Gebert, M. Buzzi, G. Jotzu, E. Wang, T. Matsuyama, G. Meier, Y. Laplace, D. Pontiroli, M. Riccò, F. Schlawin, D. Jaksch, and A. Cavalleri, Evidence for metastable photo-induced superconductivity in K_3C_{60}, Nat. Phys. **17**, 611 (2021).

[12] A. Kogar, A. Zong, P. E. Dolgirev, X. Z. Shen, J. Straquadine, Y. Q. Bie, X. R. Wang, T. Rohwer, I. C. Tung, Y. F. Yang, R. K. Li, J. Yang, S. Weathersby, S. J. Park, M. E. Kozina, E. J. Sie, H. D. Wen, P. J. Herrero, I. R. Fisher, X. J. Wang, and N. Gedik, Light-induced charge density wave in $LaTe_3$, Nat. Phys. **16**, 159 (2020).

[13] S. Wandel, F. Boschini, E. H. da Silva Neto, L. Shen, M. X. Na, S. Zohar, Y. Wang, S. B. Welch, M. H. Seaberg, J. D. Koralek, G. L. Dakovski, W. Hettel, M. F. Lin, S. P. Moeller, W. F. Schlotter, A. H. Reid, M. P. Minitti, T. Boyle, F. He, R. Sutarto *et al.*, Enhanced charge density wave coherence in a light-quenched high-temperature superconductor, Science **376**, 860 (2022).

[14] T. F. Nova, A. S. Disa, M. Fechner, and A. Cavalleri, Metastable ferroelectricity in optically strained $SrTiO_3$, Science **364**, 1075 (2019).

[15] X. Wang, C. X. Xiao, H. Park, J. Y. Zhu, C. Wang, T. Taniguchi, K. J. Watanabe, J. Q. Yan, D. Xiao, D. R. Gamelin, W. Yao, and X. D. Xu, Light-induced ferromagnetism in moiré superlattices, Nature (London) **604**, 468 (2022).

[16] M. Z. Mo, Z. Chen, R. K. Li, M. Dunning, B. B. L. Witte, J. K. Baldwin, L. B. Fletcher, J. B. Kim, A. Ng, R. Redmer, A. H. Reid, P. Shekhar, X. Z. Shen, M. Shen, K. Sokolowski-Tinten, Y. Y. Tsui, Y. Q. Wang, Q. Zheng, X. J. Wang, and S. H. Glenzer, Heterogeneous to homogeneous melting transition visualized with ultrafast electron diffraction, Science **360**, 1451 (2018).

[17] G. Sciaini and R. J. D. Miller, Femtosecond electron diffraction: Heralding the era of atomically resolved dynamics, Rep. Prog. Phys. **74**, 096101 (2011).

[18] A. M. Lindenberg, J. Larsson, K. Sokolowski-Tinten, K. J. Gaffney, C. Blome, O. Synnergren, J. Sheppard, C. Caleman, A. G. MacPhee, D. Weinstein, D. P. Lowney, T. K. Allison, T. Matthews, R. W. Falcone, A. L. Cavalieri, D. M. Fritz, S. H. Lee, P. H. Bucksbaum, D. A. Reis, J. Rudati *et al.*, Atomic-scale visualization of inertial dynamics, Science **308**, 392 (2005).

[19] L. Chen, A. Y. Cui, M. Li, S. B. Li, S. J. Gong, K. Jiang, J. Z. Zhang, L. Q. Zhu, L. Y. Shang, Y. W. Li, Z. G. Hu, and J. H. Chu, Optical excitation-induced ultrafast amorphization in the Y-Sb-Te alloy system: Insights from real-time time-dependent DFT with molecular dynamics calculations, Phys. Rev. B **106**, 214110 (2022).

[20] W. B. Chu, S. J. Tan, Q. J. Zheng, W. Fang, Y. X. Feng, O. V. Prezhdo, B. Wang, X. Z. Li, and J. Zhao, Ultrafast charge transfer coupled to quantum proton motion at molecule/metal oxide interface, Sci. Adv. **8**, eabo2675 (2022).

[21] W. H. Liu, Y. X. Gu, Z. Wang, S. S. Li, L. W. Wang, and J. W. Luo, Origin of immediate damping of coherent oscillations in photoinduced charge-density-wave transition, Phys. Rev. Lett. **130**, 146901 (2023).

[22] M. X. Guan, X. B. Liu, D. Q. Chen, X. Y. Li, Y. P. Qi, Q. Yang, P. W. You, and S. Meng, Optical control of multistage phase transition via phonon coupling in $MoTe_2$, Phys. Rev. Lett. **128**, 015702 (2022).

[23] C. Lian, Z. A. Ali, H. Kwon, and B. M. Wong, Indirect but efficient: Laser-excited electrons can drive ultrafast polarization switching in ferroelectric materials, J. Phys. Chem. Lett. **10**, 3402 (2019).

[24] F. Y. Gu, É. Murray, and P. Tangney, Carrier-mediated control over the soft mode and ferroelectricity in $BaTiO_3$, Phy. Rev. Mater. **5**, 034414 (2021).

[25] F. Rao, K. Ding, Y. Zhou, Y. Zheng, M. Xia, S. Lv, Z. Song, S. Feng, I. Ronneberger, R. Mazzarello, W. Zhang, and E. Ma, Reducing the stochasticity of crystal nucleation to enable subnanosecond memory writing, Science **358**, 1423 (2017).

[26] W. Zhang, R. Mazzarello, M. Wuttig, and E. Ma, Designing crystallization in phase-change materials for universal memory and neuro-inspired computing, Nat. Rev. Mater. **4**, 150 (2019).

[27] X. Z. Chen, Y. Xue, Y. B. Sun, J. B. Shen, S. N. Song, M. Zhu, Z. T. Song, Z. G. Cheng, and P. Zhou, Neuromorphic photonic memory devices using ultrafast nonvolatile phase-change materials, Adv. Mater. **35**, 2203909 (2023).

[28] M. Wuttig, H. Bhaskaran, and T. Taubner, Phase-change materials for non-volatile photonic applications, Nat. Photonics **11**, 465 (2017).

[29] X. P. Wang, X. B. Li, N. K. Chen, Q. D. Chen, X. D. Han, S. B. Zhang, and H. B. Sun, Element-specific amorphization of vacancy-ordered GeSbTe for ternary-state phase change memory, Acta Mater. **136**, 242 (2017).

[30] T. Matsunaga, J. Akola, S. Kohara, T. Honma, K. Kobayashi, E. Ikenaga, R. O. Jones, N. Yamada, M. Takata, and R. Kojima, From local structure to nanosecond recrystallization dynamics in AgInSbTe phase-change materials, Nat. Mater. **10**, 129 (2011).

[31] C. Qiao, K. W. Bai, M. Xu, S. Y. Wang, C. Z. Wang, K. M. Ho, X. S. Miao, and M. Xu, Ultrafast crystallization mechanism of amorphous $Ge_{15}Sb_{85}$ unraveled by pressure-driven simulations, Acta Mater. **216**, 117123 (2021).

[32] M. Micoulaut and H. Flores-Ruiz, Rules of hierarchical melt and coordinate bond to design crystallization in doped phase change materials, Phys. Rev. B **103**, 134206 (2021).

[33] X. B. Li, X. Q. Liu, X. Liu, D. Han, Z. Zhang, X. D. Han, H. B. Sun, and S. B. Zhang, Role of electronic excitation in the amorphization of Ge-Sb-Te alloys, Phys. Rev. Lett. **107**, 015501 (2011).

[34] L. Waldecker, T. A. Miller, M. Rudé, R. Bertoni, J. Osmond, V. Pruneri, R. E. Simpson, R. Ernstorfer, and S. Wall, Time-domain separation of optical properties from structural transitions in resonantly bonded materials, Nat. Mater. **14**, 991 (2015).

[35] Y. P. Qi, N. K. Chen, T. Vasileiadis, D. Zahn, H. Seiler, X. B. Li, and R. Ernstorfer, Photoinduced ultrafast transition of the local correlated structure in chalcogenide phase-change materials, Phys. Rev. Lett. **129**, 135701 (2022).

[36] M. Wuttig, and N. Yamada, Phase-change materials for rewriteable data storage, Nat. Mater. **6**, 824 (2007).

[37] W. L. Jia, J. Lang, X. B. Chi, and L. W. Wang, GPU implementation of the linear scaling three dimensional fragment method for large scale electronic structure calculations, Comput. Phys. Commun. **211**, 8 (2017).

[38] W. H. Liu, J. W. Luo, S. S. Li, and L. W. Wang, Microscopic force driving the photoinduced ultrafast phase transition: Time-dependent density functional theory simulations of $IrTe_2$, Phys. Rev. B **102**, 184308 (2020).

[39] Z. Wang, S. S. Li, and L. W. Wang, Efficient real-time time-dependent density functional theory method and its application to a collision of an ion with a 2D material, Phys. Rev. Lett. **114**, 063004 (2015).

[40] D. R. Hamann, Erratum: Optimized norm-conserving Vanderbilt pseudopotentials, Phys. Rev. B **88**, 085117 (2013).

[41] Z. W. Nie, Y. X. Wang, D. Q. Chen, and S. Meng, Unraveling hidden charge density wave phases in $1T$-$TiSe_2$, Phys. Rev. Lett. **131**, 196401 (2023).

[42] J. J. Li, Y. P. Qi, Q. Yang, L. Y. Yue, C. Y. Yao, Z. J. Chen, S. Meng, D. Xiang, and J. M. Cao, Femtosecond electron diffraction reveals local disorder and local anharmonicity in thermoelectric SnSe, Adv. Mater. **36**, 2313742 (2024).

[43] N. Wu, S. J. Zhang, D. Q. Chen, Y. X. Wang, and S. Meng, Three-stage ultrafast demagnetization dynamics in a monolayer ferromagnet, Nat. Commun. **15**, 2804 (2024).

[44] R. J. Zhao, P. W. You, and S. Meng, Ring polymer molecular dynamics with electronic transitions, Phys. Rev. Lett. **130**, 166401 (2023).

[45] X. B. Liu, S. Q. Hu, D. Q. Chen, M. X. Guan, Q. Chen, and S. Meng, Calibrating out-of-equilibrium electron-phonon couplings in photoexcited MoS_2, Nano Lett. **22**, 4800 (2022).

[46] W. H. Liu, J. W. Luo, and S. S. Li, The critical role of hot carrier cooling in optically excited structural transitions, npj Comput. Mater. **7**, 117 (2021).

[47] L. Chen, L. Wang, K. Jiang, J. Z. Zhang, Y. W. Li, L. Y. Shang, L. Q. Zhu, S. J. Gong, and Z. G. Hu, Optically induced multistage phase transition in coherent phonon-dominated a-GeTe, J. Phys. Chem. Lett. **14**, 5760 (2023).

[48] C. Lian, S. B. Zhang, and S. Meng, *Ab initio* evidence for nonthermal characteristics in ultrafast laser melting, Phys. Rev. B **94**, 184310 (2016).

[49] E. S. Zijlstra, A. Kalitsov, T. Zier, and M. E. Garcia, Squeezed thermal phonons precurse nonthermal melting of silicon as a function of fluence, Phys. Rev. X **3**, 011005 (2013).

[50] J. Bang, Y. Y. Sun, X. Q. Liu, F. Gao, and S. B. Zhang, Carrier-multiplication-induced structural change during ultrafast carrier relaxation and nonthermal phase transition in semiconductors, Phys. Rev. Lett. **117**, 126402 (2016).

[51] T. Frigge, B. Hafke, T. Witte, B. Krenzer, C. Streübhr, A. Samad Syed, V. Mikšić Trontl, I. Avigo, P. Zhou, M. Ligges, D. von der Linde, U. Bovensiepen, M. H. Hoegen, S. Wippermann, A. Lücke, S. Sanna, U. Gerstmann, and W. G. Schmidt, Optically excited structural transition in atomic wires on surfaces at the quantum limit, Nature (London) **544**, 207 (2017).

[52] N. K. Chen, J. Bang, X. B. Li, X. P. Wang, D. Wang, Q. D. Chen, H. B. Sun, and S. B. Zhang, Optical subpicosecond nonvolatile switching and electron-phonon coupling in ferroelectric materials, Phys. Rev. B **102**, 184115 (2020).

[53] E. Matsubara, S. Okada, T. Ichitsubo, T. Kawaguchi, A. Hirata, P. F. Guan, K. Tokuda, K. Tanimura, T. Matsunaga, M. W. Chen, and N. Yamada, Initial atomic motion immediately following femtosecond-laser excitation in phase-change materials, Phys. Rev. Lett. **117**, 135501 (2016).

[54] N. K. Chen, X. B. Li, J. Bang, X. P. Wang, D. Han, D. West, S. Zhang, and H. B. Sun, Directional forces by momentumless excitation and order-to-order transition in Peierls-distorted solids: The case of GeTe, Phys. Rev. Lett. **120**, 185701 (2018).

[55] T. A. Miller, M. Rudé, V. Pruneri, and S. Wall, Ultrafast optical response of the amorphous and crystalline states of the phase change material $Ge_2Sb_2Te_5$, Phys. Rev. B **94**, 024301 (2016).

[56] A. Marini, C. Hogan, M. Grüning, and D. Varsano, yambo: An *ab initio* tool for excited state calculations, Comput. Phys. Commun. **180**, 1392 (2009).

[57] X. Andrade, J. A. Rodriguez, D. A. Strubbe, M. J. T. Oliveira, F. Nogueira, and A. Castro, Time-dependent density-functional theory in massively parallel computer architectures: The OCTOPUS project, J. Phys.: Condens. Matter **24**, 233202 (2012).

[58] G. Kolesov, O. Granas, R. Hoyt, D. Vinichenko, and E. Kaxiras, Real-time TD-DFT with classical ion dynamics: Methodology and applications, J. Chem. Theory Comput. **12**, 466 (2016).

[59] J. Ren, N. Vukmirović, and L. W. Wang, Phys. Rev. B **87**, 205117 (2013).

[60] J. Kang and L. W. Wang, Nonadiabatic molecular dynamics simulation for carrier transport in a pentathiophene butyric acid monolayer, Phys. Rev. B **99**, 224303 (2019).

[61] L. W. Wang, Natural orbital branching scheme for time-dependent density functional theory nonadiabatic simulations, J. Phys. Chem. A **124**, 9075 (2020).

[62] F. Zheng and L. W. Wang, Ultrafast hot carrier injection in Au/GaN: The role of band bending and the interface band structure, J. Phys. Chem. Lett. **10**, 6174 (2019).

[63] K. Sokolowski-Tinten, J. Bialkowski, and D. V. Linde, Ultra-fast laser-induced order-disorder transitions in semiconductors, Phys. Rev. B **51**, 14186 (1995).

[64] K. Shportko, S. Kremers, M. Woda, D. Lencer, J. Robertson and M. Wuttig, Resonant bonding in crystalline phase-change materials, Nat. Mater. **7**, 653 (2008).

[65] D. K. Gramotnev and S. I. Bozhevolnyi, Plasmonics beyond the diffraction limit, Nat. Photonics **4**, 83 (2010).

[66] Q. Yin and L. Chen, Enhanced optical properties of Sn-doped $Ge_2Sb_2Te_5$ thin film with structural evolution, J. Alloys Compd. **770**, 692 (2019).

[67] B. Lee, J. R. Abelson, S. G. Bishop, D. Kang, B. Cheong, and K. Kim, Investigation of the optical and electronic properties of phase change material in its amorphous, cubic, and hexagonal phases, J. Appl. Phys. **97**, 093509 (2005).

[68] C. Steimer, V. Coulet, W. Welnic, H. Dieker, R. Detemple, C. Bichara, B. Beuneu, J. P. Gaspard, and M. Wuttig, Characteristic ordering in liquid phase-change materials, Adv. Mater. **20**, 4535 (2008).

[69] J. Y. Raty, W. Zhang, J. Luckas, C. Chen, C. Bichara, R. Mazzarello and M. Wuttig, Aging mechanisms in amorphous phase-change materials, Nat. Commun. **6**, 7467 (2015).

[70] W.-H. Liu, J.-W. Luo, S.-S. Li, and L.-W. Wang, The seeds and homogeneous nucleation of photoinduced nonthermal melting in semiconductors due to self-amplified local dynamic instability, Sci. Adv. **8**, eabn4430 (2022).